Measurement of the ^{239}Pu(n, f) cross section from 4 keV to 100 MeV using the white neutron source at the CSNS Back-n facility

Yijia Qiu,[1] Changlin Lan,[1,*] Yonghao Chen,[2,3,†] Liyang Jiang,[4] Jie Bao,[4] Yiwei Yang,[5] Zhongwei Wen,[5] Rong Liu,[5] Xichao Ruan,[4] Jingyu Tang,[2,3] Jie Ren,[4] Hantao Jing,[2,3] Guangyuan Luan,[4] Ruirui Fan,[2,3] Yangbo Nie,[4] Xianlin Yang,[1] Xiaojun Li,[1] Han Yi,[2,3] Wei Jiang,[2,3] Tao Ye,[6] Yi Yang,[4] Shilong Liu,[4] and Jincheng Wang[4]

[1]*School of Nuclear Science and Technology, Lanzhou University, Lanzhou 730000, China*

[2]*Institute of High Energy Physics, Chinese Academy of Sciences (CAS), Beijing 100049, China*

[3]*Spallation Neutron Source Science Center, Dongguan 523803, China*

[4]*Key Laboratory of Nuclear Data, China Institute of Atomic Energy, Beijing 102413, China*

[5]*Institute of Nuclear Physics and Chemistry, China Academy of Engineering Physics, Mianyang 621900, China*

[6]*Institute of Applied Physics and Computational Mathematics, Beijing 100088, China*

(Received 10 March 2022; accepted 25 January 2023; published 13 February 2023)

The neutron-induced fission cross section of ^{239}Pu was measured relative to ^{235}U(n, f) at the back-streaming white neutron beam line (Back-n) of the China Spallation Neutron Source (CSNS). A multicell fast fission ionization chamber was used to perform the measurement. The reliability of the measurement was verified by the high consistency of ^{235}U's resonances between the measurement and the evaluation data. The ^{239}Pu fission cross sections from 4 keV to 100 MeV are obtained with 1.7–5.8 % uncertainty when unfolding uncertainties are excluded. The total uncertainties including the unfolding errors, which reflect the effect of the double-bunch unfolding method, are 2.6–15 % from 10 keV to 100 MeV.

DOI: 10.1103/PhysRevC.107.024606

I. INTRODUCTION

Neutron-induced fission cross section is one of the most important data for nuclear energy production, which is supposed to be more clean, sustainable, and safe. In the U-Pu cycle, ^{239}Pu is produced through neutron capture of ^{238}U, followed by two successive β^- decays. The fission of ^{239}Pu generates a substantial fraction of the energy production in a reactor, owing to the breeding process during irradiation. The fast reactor sensitivity studies need ^{239}Pu fission cross section with low uncertainty [1]. Therefore, reducing the uncertainties of the ^{239}Pu(n, f) cross section is of interest, particularly in the fast neutron region.

The fission cross section of ^{239}Pu has been measured extensively in a wide energy range for nuclear applications. However, only four measurements have extended neutron energies above 30 MeV. They are measurements by Carlson *et al.* [2] at the Lawrence Livermore National Laboratory up to 30 MeV, by Staples *et al.* [3] at the Weapons Neutron Research up to 400 MeV, by Shcherbakov *et al.* [4] at the neutron spectrometer GNEIS up to 200 MeV, and by Tovesson *et al.* [5] at the Los Alamos Neutron Science Center up to 200 MeV. Nevertheless, these data exhibit discrepancies up to 10% when the neuron energy is above 10 MeV.

In this paper, the measurement performed at the back-streaming white neutron beam line (Back-n) of the China Spallation Neutron Source (CSNS) is presented and the results of ^{239}Pu(n, f) cross sections from 4 keV to 100 MeV are shown.

II. EXPERIMENTAL METHOD

The neutron-induced fission cross section of ^{239}Pu can be determined relative to ^{235}U(n, f) according to Eq. (1):

$$\sigma^{\mathrm{Pu}}(E_n) = \sigma^{\mathrm{U}}(E_n)\frac{C^{\mathrm{Pu}}(E_n)}{C^{\mathrm{U}}(E_n)}\frac{\varepsilon^{\mathrm{U}}(E_n)}{\varepsilon^{\mathrm{Pu}}(E_n)}\frac{N_s^{\mathrm{U}}}{N_s^{\mathrm{Pu}}}K(E_n), \tag{1}$$

where $\sigma(E_n)$ is the fission cross section at neutron energy E_n, the superscripts Pu and U refer to the ^{239}Pu and ^{235}U samples, respectively, C is the measured fission event, ε is the detection efficiency of the fission events, N_s is the areal density (atoms/barn) of the sample, and K represents the correction factor:

$$K(E_n) = \frac{k_{ic}^{\mathrm{Pu}}(E_n)}{k_{ic}^{\mathrm{U}}(E_n)}\frac{k_{nfa}^{\mathrm{Pu}}(E_n)}{k_{nfa}^{\mathrm{U}}(E_n)} \tag{2}$$

Here, k_{ic} is the correction for isotope composition, k_{nfa} is the correction for neutron flux attenuation. Details of these corrections are described in Sec. IV.

III. EXPERIMENTAL SETUP

A. Neutron source

CSNS is producing neutrons by impinging 1.6 GeV protons on a thick tungsten target. The Back-n was exploited mainly for the nuclear data measurement [6–9].

*Corresponding author: lanchl@lzu.edu.cn

†Corresponding author: chenyonghao@ihep.ac.cn

 ©2023 American Physical Society

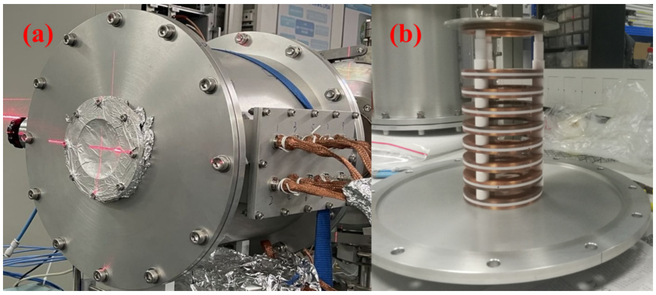

FIG. 1. Photo of the FIXM (a) and its inside structure (b).

This measurement was performed in the double-bunch mode for about 100 h at endstation 1 (with a flight path about 57 m). The CSNS accelerator complex is usually operated in double-bunch mode, which means in one pulse there are two identical proton bunches with a fixed interval of 410 ns. Each Gauss-type bunch has a length of about 60 ns (FWHM).

The beam spot for this measurement was simulated by FLUKA, which can be considered as an ellipse with 62 mm major axis and 58 mm minor axis (full width at tenth maximum). The neutron flux at different samples is normalized by sample active area.

B. Detector and data acquisition

A fast fission ionization chamber for the fission cross section measurement (FIXM) was mounted at the endstation 1 of Back-n. The chamber is a ϕ300 mm × 300 mm cylinder made of 5 mm-thick aluminium alloy. The neutron window (ϕ80 mm) was sealed with 100 µm Kapton film at the center of chamber caps [10]. The chamber was filled with a mixture gas of 90% Ar and 10% CF_4 at a pressure of 800 mbar. A stack of fission cells was mounted inside the chamber along the neutron beam direction. The structure of the FIXM is shown in Fig. 1.

Each fission cell consists of two ϕ80 mm electrodes. The aluminum anode for collecting signals was connected to a preamplifier, while the cathode electrode plated with the sample material was connected to the ground. A 5-mm-wide gap and a high voltage of +200 V between electrodes were designed in order to give electrons enough drift velocity. An eight-channel preamplifier was connected to the chamber and delivered signals to the data acquisition system (DAQ) [11]. The DAQ digitized signal waveforms with 12-bit resolution and 1 GHz sampling rate. The DAQ time windows were set to 10 ms for the uranium samples and 5 ms for the plutonium samples, respectively.

C. Samples

Two uranium and two plutonium samples were used in this measurement, which were ^{235}U-5, ^{235}U-1, ^{239}Pu-1, and ^{239}Pu-2, respectively. The plutonium samples were electroplated on platinum backings. The uranium samples were electroplated on the stainless steel backing for ^{235}U-1 and the aluminium backing for ^{235}U-5, respectively. The diameter of the active area of the uranium samples is about 50 mm, while the diameter of plutonium samples is about 25.4 mm. The sample masses were determined by the α-particle spectra measured with a silicon detector in a small solid angle device. The details of the samples are listed in Table I in order of the placement in the FIXM chamber. The isotopic abundances of the ^{235}U and ^{239}Pu samples are respectively listed in Tables II and III. Unfortunately, the uncertainty of the isotopic abundances of the ^{239}Pu are not known since they are aged samples which were made in the 1970s.

TABLE I. The details of the samples used in the measurement.

Cell ID	Sample	Mass (μg)	Diameter (mm)	Backing
1	^{235}U-5	6319	49.88	Al
2	^{239}Pu-1	373	25.4	Pt + Al
3	^{239}Pu-2	401	25.4	Pt + Al
4	^{235}U-1	5173	49.74	stainless steel

IV. DATA ANALYSIS

A. Raw data treatment

A dedicated routine was developed to treat the raw data based on the ROOT [12] software package. The raw data of Back-n contain the full waveforms of the detector signals so that the information of the desired signals can be extracted. A dedicated routine was developed to treat the raw data of the FIXM [9], which calculated the derivative of the original signal and the zero-crossing method was used to define the timing and the amplitude.

The first two signals in Fig. 2(a) are γ-flash signals, and the third is a typical fission fragment (FF) signal. Figure 2(b) shows their derivatives. The two blue dashed lines are the thresholds set for the derivative signal. Signals crossing two thresholds with a lower-lower-upper-upper sequence are selected out. The zero-crossing time is defined as the timing of the signal, while the peak-to-peak value is defined as the amplitude since it is proportional to the amplitude of the original signal.

B. Neutron-energy calibration

The incident neutron energy, determined by the time-of-flight (TOF) method, can be calculated by

$$E_n = (\gamma - 1)m_n c^2, \tag{3}$$

TABLE II. Isotopic abundance of the ^{235}U sample

Isotope	Abundance (%)	Uncertainty (%)
^{234}U	1.26×10^{-3}	1.25×10^{-1}
^{235}U	99.985	6.75×10^{-6}
^{236}U	4.12×10^{-3}	1.19×10^{-1}
^{238}U	9.63×10^{-3}	2.91×10^{-2}

TABLE III. Isotopic abundance of the ^{239}Pu sample

Isotope	Abundance (%)
^{239}Pu	96.71
^{240}Pu	3.14
^{241}Am	0.15

where E_n is the incident neutron energy, c is the speed of light, m_n is the neutron mass, and γ is calculated by

$$\gamma = \frac{1}{\sqrt{1-\left(\frac{v}{c}\right)^2}}, \quad v = \frac{L}{\mathrm{TOF}}, \tag{4}$$

where v is the neutron velocity and L is the flight path. The TOF is calculated by

$$\mathrm{TOF} = T - T_g + \mathrm{TOF}_g, \tag{5}$$

where T is the timing of the FFs recorded by the detector, T_g is the timing of the first γ-flash signal, $\mathrm{TOF}_g = L/c$ is the TOF of the γ flash from the spallation target to the detector. The γ-flash signal is not saturated in this experiment, since the ionization chamber is not sensitive to γ rays and the γ flash is quite weaker in back direction than that of in the forward direction. Therefore it can be used as a good reference for calibrating the TOF. L was determined by comparing the resonance peak at 8.77 eV between the measurement and the evaluation data, as shown in Fig. 3. The L of the ^{235}U-5 sample is calibrated as 56.973 m in this measurement.

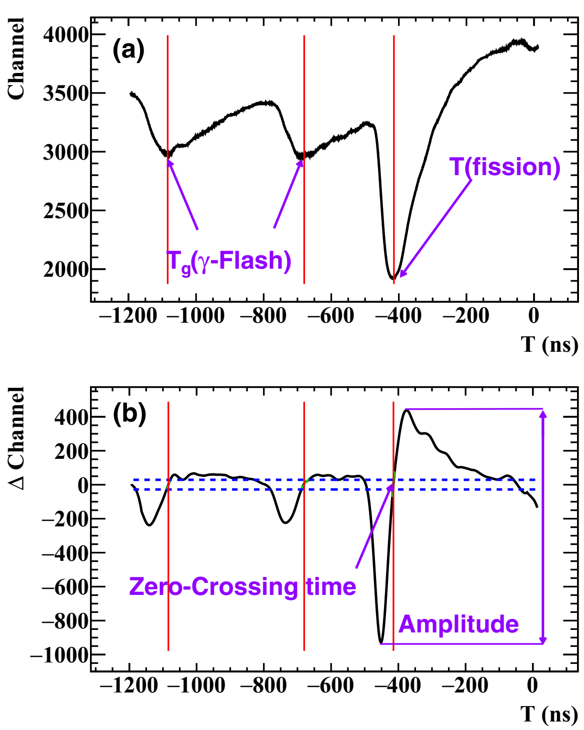

FIG. 2. Signal frame including γ-flash signals and a FF signal (a) and their derivatives (b). The red solid line corresponds to zero-crossing time and the two blue dashed lines correspond to the two thresholds.

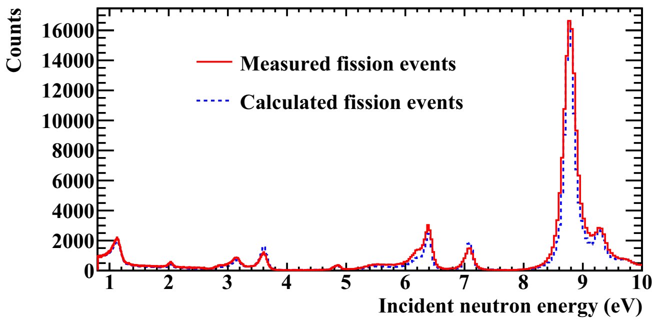

FIG. 3. Comparison between the measured fission events of ^{235}U and its fission cross section from ENDF/B-VIII.0.

A two-dimensional (2D) distribution of the neutron energy vs the signal amplitude is shown in Fig. 4. A large number of events with much lower amplitudes are mainly α particles emitted from the ^{239}Pu sample. When the neutron energy is above 10 MeV, the charged particles from (n, x) reactions between neutron and the sample or backing will increase lower-amplitude events. After cutting off lower-amplitude events, we can obtain the fission events of ^{239}Pu as a function of the neutron TOF and energy with 50 bins per decade (bpd) as shown in Fig. 5.

C. Double-bunch unfolding

Due to the superposition of the event distributions corresponding to the double-bunch operation mode, the resolution of the TOF measurement at Back-n will be deteriorated, especially in the high neutron energy region. Since there is no preferred sequence between the two bunches when they are extracted from the synchrotron, the accumulated double-bunch distribution can be treated as the superposition of two identical single-bunch distributions with a delay of 410 ns. An unfolding algorithm based on the Bayesian theorem was used to solve this problem [13]. The Bayesian unfolding iterative algorithm can be written as

$$C_i^{(k+1)} = E_i \frac{C_i^{(k)}}{C_{i-\Delta}^{(k)} + C_i^{(k)}} + E_{i+\Delta} \frac{C_i^{(k)}}{C_i^{(k)} + C_{i+\Delta}^{(k)}}, \tag{6}$$

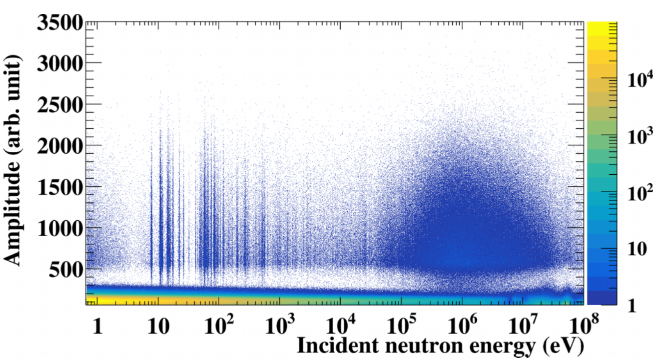

FIG. 4. 2D distribution of neutron energy vs amplitude for a ^{239}Pu sample.

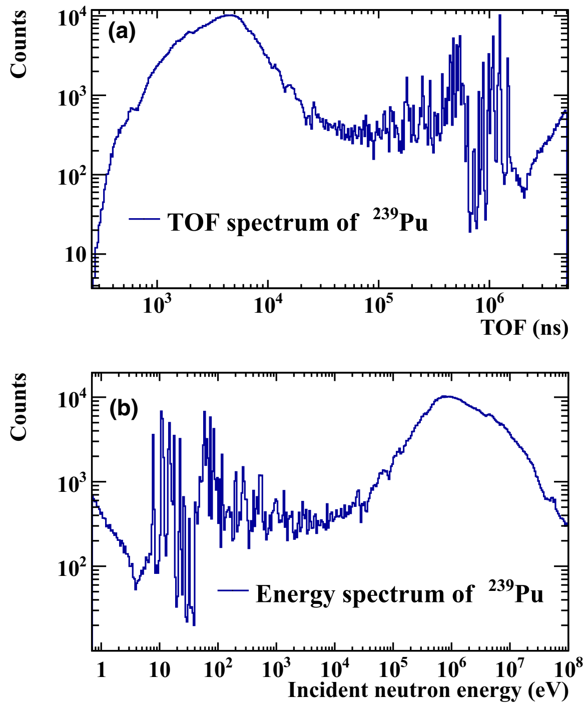

FIG. 5. The fission events of ^{239}Pu as a function of neutron TOF (a) and energy (b) with 50 bpd.

where E_i is the count of the ith TOF bin in double-bunch mode, C_i is the ith bin count in the case of single-bunch mode, Δ is the number of bins corresponding to the offset of 410 ns

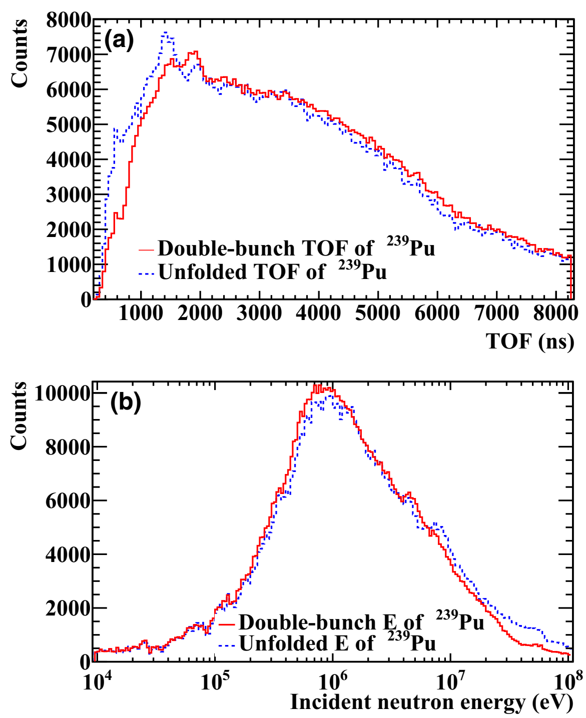

FIG. 6. Before-and-after comparisons of the ^{239}Pu fission TOF (a) and energy (b) spectrum by using Bayesian unfolding method.

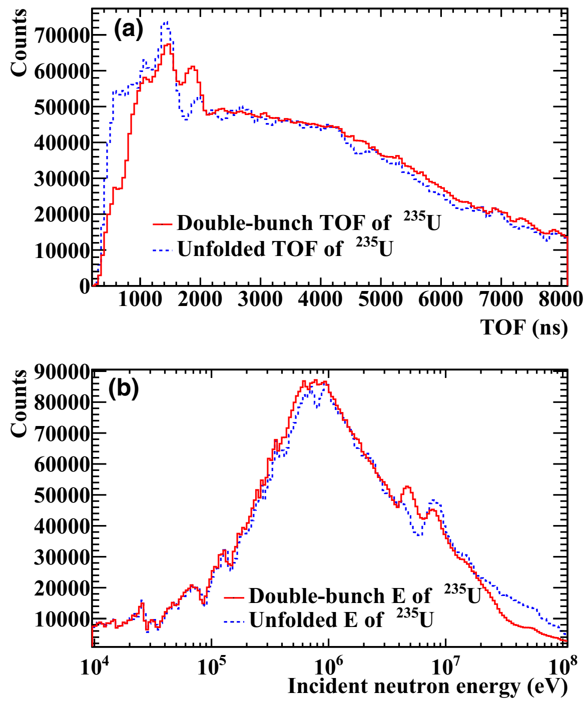

FIG. 7. Before-and-after comparisons of the ^{235}U fission TOF (a) and energy (b) spectrum by using Bayesian unfolding method.

($\Delta = 410\,\mathrm{ns}/w$, w is the bin width), the superscript k means the kth iteration. The criterion of stopping the iteration can be determined by the likelihood maximization method. The reliability and accuracy of the unfolding program have been tested with simulated data and experimental data.

The unfolding method is only used at the neutron energy above 10 keV. Event distributions are improved by using the unfolding method, especially in the multi-chance fission energy range, as shown in Figs. 6 and 7 which are corresponding to ^{239}Pu and ^{235}U, respectively.

D. Detector efficiency determination

The detection efficiency loss of the FF is mainly dominated by the two factors. First, the FFs generated inside the sample may lose all their energies and stop in the sample.

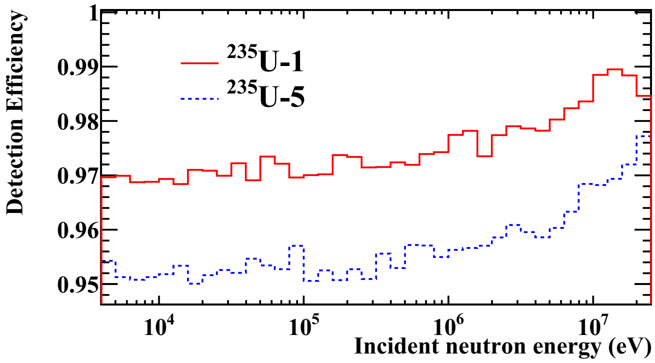

FIG. 8. Detection efficiency due to FF self-absorption simulated by GEANT4.

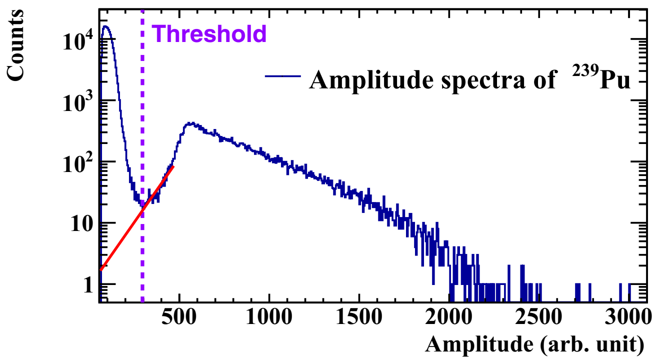

FIG. 9. The distribution of signal amplitude of ^{239}Pu and its fission event threshold cut at neutron energy above 20 MeV.

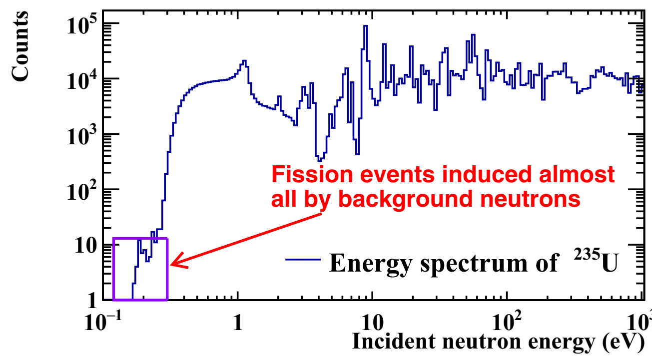

FIG. 10. The fission events of ^{235}U as a function of neutron energy with 50 bpd.

This part of the efficiency loss can be simulated by Monte Carlo (MC) method. The effect of the FF angular distribution was taken into account in simulation by using parametric modeling in GEANT4 [14]. The simulated detection efficiency due to FF self-absorption $\varepsilon_{\mathrm{FF}sa}$ is shown in Fig. 8, which is calculated by

$$\varepsilon_{\mathrm{FF}sa} = \frac{C_{\mathrm{FFin}}}{C_{\mathrm{FF}}}, \tag{7}$$

where C_{FFin} represents the fission events can be detected in ionization chamber, C_{FF} represents the fission events produced in the sample.

Second, the threshold cut set for the fission event causes the efficiency loss, too. It can be deduced based on the amplitude distribution. The fission event threshold cut was determined to be above the maximum amplitude of α particles. Figure 9 shows the event amplitude distribution of the ^{239}Pu at the neutron energy above 20 MeV. An exponential fit above the threshold was applied and extrapolated to estimate the fission events under the threshold, from which the loss rate ε_{Ftc} can be estimated. Detection efficiency due to the threshold cut of different samples in different energy ranges are listed in Table IV. As one can see, the efficiency due to the threshold cut is varying little with the neutron energy.

E. Background estimation

As a 1 mm thick cadmium filter was placed at the neutron beam window to cut off the neutrons below 0.3 eV, the fission events, whose corresponding neutron energy are lower than this energy edge, are actually induced by the background neutrons. According to the time windows of DAQ and flight path, the lowest neutron energy that can be detected at endstation 1 is 0.17 eV. Therefore the background contribution can be estimated by measuring the fission events in the neutron energy range from 0.17 eV to 0.3 eV. As shown in Fig. 10, the fission events in this neutron energy range are so few that the contribution from the background is negligible.

TABLE IV. Detection efficiency due to the threshold cut of the different samples in the different neutron energy ranges.

Neutron energy range	Detection efficiency due to the threshold cut			
	^{235}U-5	^{239}Pu-1	^{239}Pu-2	^{235}U-1
$E_n \leqslant 100$ keV	97.65%	98.70%	98.64%	97.80%
100 keV$<E_n \leqslant 1$ MeV	98.06%	98.52%	97.65%	97.81%
1 MeV$< E_n \leqslant 20$ MeV	98.01%	98.53%	97.87%	98.75%
$E_n >20$ MeV	97.67%	96.32%	96.51%	97.73%

F. Neutron flux attenuation

The neutron beam may be attenuated when it penetrates the materials (entrance window, electrodes and sample backings). A GEANT4 simulation was done to study this effect. The geometric model for simulation was built based on the detector structure, as shown in Fig. 1. The transmission rate of the neutron flux shown in Fig. 11 indicates the attenuation. One can see that the flux attenuation tends to be more severe, especially in the low-energy region with the increase of the material amount. The dips and fluctuations are due to the absorption of the samples and their backings.

G. Isotope correction

Fission events from other isotopes contribute to the measured fission events as well, since the plutonium samples are not highly enriched. The percentage of the fission events from the desired isotope can be determined based on the isotope

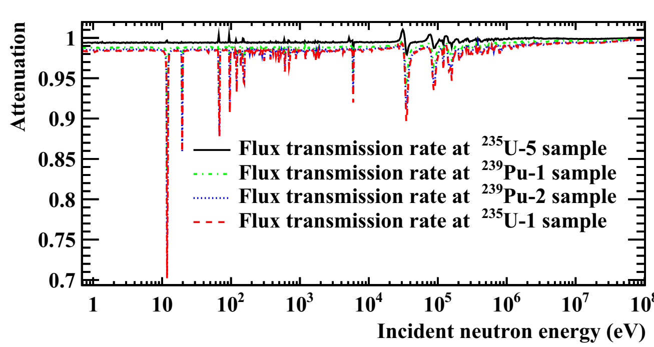

FIG. 11. Neutron flux transmission rate at the ^{239}Pu samples and the ^{235}U samples in FIXM.

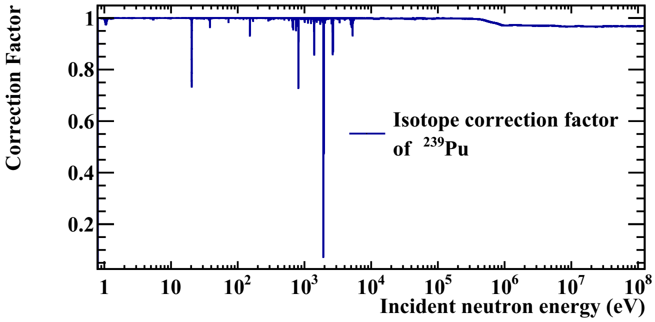

FIG. 12. Distribution of the isotope correction factor for the ^{239}Pu isotope.

composition and their fission cross sections by

$$k_{ic} = \frac{\eta_M \sigma_M}{\sum \eta_i \sigma_i}, \tag{8}$$

where η is the abundance of the isotope, σ is the fission cross section retrieved from the nuclear data library. The subscripts M stands for the desired isotope, while i stands for the isotope in the sample. The fission cross sections of different isotopes in different energy regions are taken from ENDF/B-VIII.0 [15], ENDF/B-VII.1 [16], JENDL/HE [17], and TENDL-2019 [18].

The correction factor as a function of neutron energy is shown in Fig. 12, which is applied to the measured fission events to extract the contribution of ^{239}Pu. The correction factor substantially keeps as 1 when the neutron energy is less than 400 keV, apart from some resonance dips. When the energy is above 400 keV, the correction factor decreases with the increasing of neutron energy and then becomes steady around 1 MeV.

H. Consistency verification

The consistency of the measurement can be checked by comparing the normalized fission rates of the different samples (same isotope), which is defined by Eq. (9):

$$C_{\text{nor}}(E_n) = \frac{C(E_n)k(E_n)}{m\varepsilon(E_n)}, \tag{9}$$

where C_{nor} is the normalized fission rate, m is the sample mass, ε is the detection efficiency, k is the correction factor as mentioned in Sec. II.

The normalized fission rate of same kind of isotope should be consistent in our case since it only depends on the fission cross section. Figures 13(a) and 13(b) are the normalized fission rates of the ^{235}U and ^{239}Pu samples, respectively. Figures 13(c) and 13(d) are the ratios of the normalized fission rates of the ^{235}U and ^{239}Pu samples. It can be seen from Fig. 13 that they are consistent with deviations less than 5% for ^{235}U from 30 eV to 100 MeV, which demonstrates the reliability of the data in this energy region. However, the consistency of ^{239}Pu is not very good, because the ^{239}Pu-2 sample was slightly curled during the experiment due to its thin backing. Therefore, only the fission events of the ^{239}Pu-1 sample were used for cross section calculation.

V. RESULTS AND DISCUSSION

A. Measured fission cross section ratio

The measured fission cross section ratio of ^{239}Pu / ^{235}U is deduced by Eq. (10):

$$\frac{\sigma^{\text{Pu}}(E_n)}{\sigma^{\text{U}}(E_n)} = \frac{C^{\text{Pu}}(E_n)}{C^{\text{U}}(E_n)} \frac{\varepsilon^{\text{U}}(E_n)}{\varepsilon^{\text{Pu}}(E_n)} \frac{N_s^{\text{U}}}{N_s^{\text{Pu}}} K(E_n), \tag{10}$$

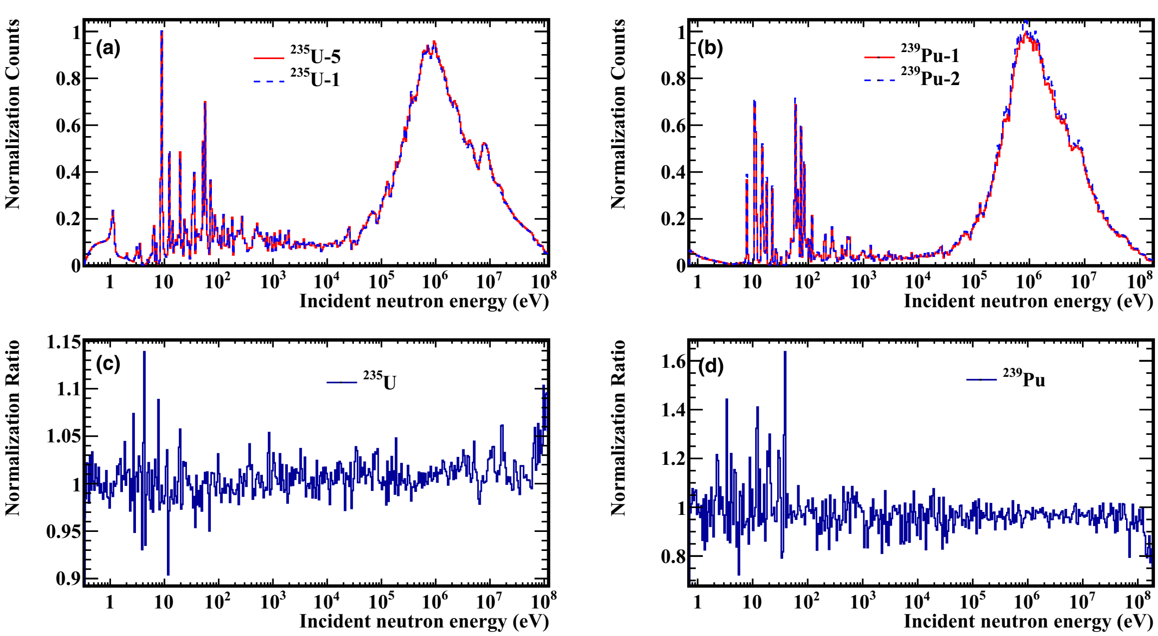

FIG. 13. Comparison of the normalized fission rate of ^{235}U and ^{239}Pu samples. (a) and (c) correspond to ^{235}U samples. (b) and (d) correspond to ^{239}Pu samples.

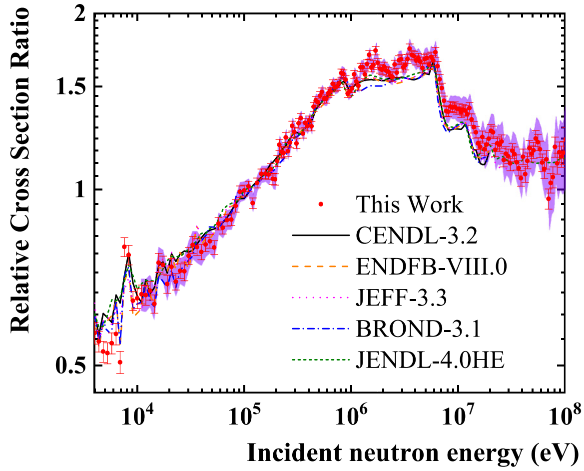

FIG. 14. Measured fission cross section ratios of ^{239}Pu / ^{235}U compared to CENDL-3.2, ENDF/B-VIII.0, JENDL-4.0/HE, JEFF-3.3, and BROND-3.1 evaluations. The violet error band corresponds to the total uncertainty including the unfolding error.

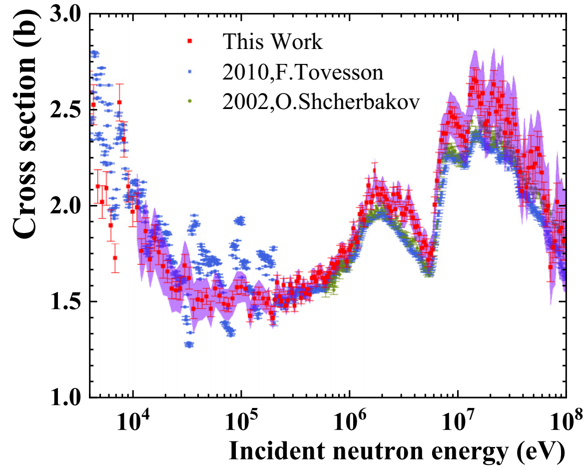

FIG. 16. Measured ^{239}Pu(n, f) cross section compared to previous data from 4 keV to 100 MeV relative to ^{235}U. The violet error band corresponds to the total uncertainty including the unfolding error.

where the fission events of ^{235}U are taken as the sum of the two samples. The obtained cross section ratios from 4 keV to 100 MeV are shown together with the evaluations in Fig. 14.

B. ^{239}Pu(n, f) cross section

The measured ^{239}Pu(n, f) cross section can be calculated based on the evaluated ^{235}U(n, f) cross section. The experimental data of this work are compared with the evaluations in Fig. 15. The black (solid), orange (dashed), pink (dotted), blue (dash-dotted), and green (densely dashed) lines, respectively, denote CENDL-3.2 [19], ENDF/B-VIII.0, JEFF3.3 [20], BROND-3.1 [21], and JENDL-4.0HE evaluations. TALYS 1.95 is also used in this work, which is a computer code that can calculate the reaction cross section based on physics models and parametrizations [22]. It calculates nuclear reactions involving target nuclides with mass >12 and projectiles, like neutrons, photons, protons, deuterons, tritons, ^{3}He, and α particles from 1 keV to 200 MeV. The calculation result is also shown in Fig. 15. The comparison with previous experimental data [4,5] is shown in Fig. 16. The determined experimental data by taking ^{235}U(n, f) cross sections as reference are in good agreement with the evaluations and other experimental data from 150 keV to 1 MeV, especially for CENDL-3.2 and BROND-3.1. In the energy range from 4 keV to 150 keV, the experimental data change more drastically with the change of the neutron energy which are in good agreement with BROND-3.1. The reason is probably that the cross section of ^{235}U(n, f) is not standard in this energy range and its excitation function is not smooth either. In the multichance fission plateaus, the experimental data of this work are higher than the evaluations, other experimental data and calculation results. Most of the experimental data of this work are varying around the JENDL-4.0HE and TALYS calculation from 30 to 80 MeV. And most of the data of this work are slightly higher than other experimental data from 30 to 65 MeV and in agreement with other experimental data from 65 to 100 MeV. Furthermore, the statistical uncertainty increases with the increasing of the neutron energy. A better time resolution and a longer measurement duration are necessary for a precise measurement in this energy region.

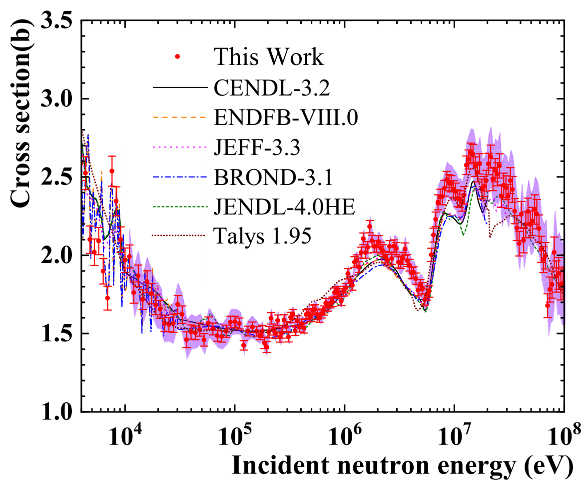

FIG. 15. Measured ^{239}Pu(n, f) cross section compared to CENDL-3.2, ENDF/B-VIII.0, JENDL-4.0/HE, JEFF-3.3, BROND-3.1 evaluations, and TALYS calculation from 4 keV to 100 MeV. The violet error band corresponds to the total uncertainty including the unfolding error.

C. Energy resolution

The relative energy resolution of a TOF facility can be calculated by

$$\frac{\Delta E}{E} = \gamma(\gamma + 1)\sqrt{\left(\frac{\Delta T}{T}\right)^2 + \left(\frac{\Delta L}{L}\right)^2}, \tag{11}$$

where γ can be calculated by Eq. (4), T and L are the TOF and the effective flight path, ΔT and ΔL are their respective

TABLE V. Relative energy resolution of CSNS Back-n at 57 m.

E_n (eV)	ΔT (ns)	ΔL (cm)	$\Delta E/E$
1	60	12.2	4.3×10^{-3}
10	60	13.6	4.8×10^{-3}
10^2	60	24.0	8.4×10^{-3}
10^3	60	20.2	7.1×10^{-3}
10^4	60	18.0	7.0×10^{-3}
10^5	60	15.4	1.07×10^{-2}
10^6	60	8.8	2.93×10^{-2}
10^7	60	10.0	9.29×10^{-2}

uncertainties. ΔT is caused by the pulse width of the proton beam which was 60 ns (FWHM) during this experiment. ΔL is caused by the moderation in the spallation target and the surrounding coolant, which can only be obtained through MC simulation [23]. According to Eq. (11), ΔT dominates the resolution at the high energy, while ΔL is dominant at low energy. The relative energy resolutions at 57 m at different energies are summarized in Table V. The energy resolution is less than 1% below 0.1 MeV and increases up to 9.3% at 10 MeV.

D. Uncertainties estimation

The uncertainties of the measured ^{239}Pu(n, f) cross sections excluding the unfolding error are all less than 5.8% and close to 1.7% near 1 MeV, as shown by the blue curve in Fig. 17. The statistical uncertainty is the main source of this uncertainty. The systematic uncertainties are mainly from the uncertainty of the ^{235}U(n, f) cross section, FF detection efficiency, and sample mass. The uncertainties of the ^{235}U(n, f) cross sections are provided by IAEA standards which vary from ∼0.6% to ∼3.6% in the range from 4 keV to 100 MeV. The uncertainty in the detection efficiency and sample mass of ^{235}U samples can be estimated by the normalized fission rate of the same isotope. However, the uncertainty in the detection efficiency and sample mass of ^{239}Pu-1 is estimated separately. The uncertainty of the detection efficiency is mainly from the threshold cut. It can be estimated by comparing the results of different fitting function, which is evaluated as ∼0.9%.

We also take into account the effect of the unfolding method to estimate the uncertainty introduced by the double-bunch operation mode. It is calculated in an iterative

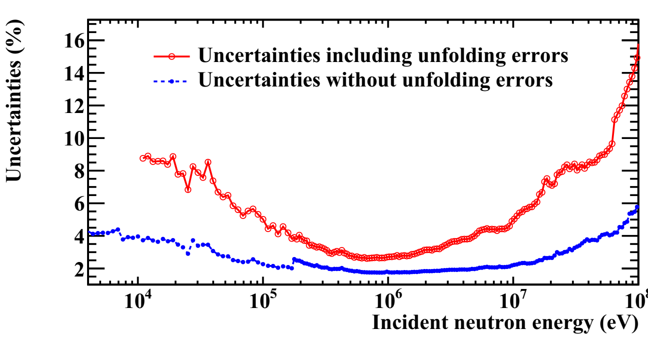

FIG. 17. The total uncertainties of measured ^{239}Pu(n, f) cross section.

way [13,24,25] and the covariances of the bin count in the unfolded distribution can be evaluated by

$$\mathrm{Cov}\left[C_i^{(k)}, C_j^{(k)}\right] = \sum_{m,n} \frac{\partial C_i^{(k)}}{\partial E_m} \frac{\partial C_j^{(k)}}{\partial E_n} \mathrm{Cov}\,[E_m, E_n]. \tag{12}$$

In each iteration, the value of the partial derivative $\partial C_i^{(k)}/\partial E_m$ or $\partial C_j^{(k)}/\partial E_n$ is stored for the error estimation in the next iteration. This iterative error estimation method can be started from the first iteration, in which $C_i^{(0)}$ is just E_i and the value of its partial derivative can be calculated directly according to Eq. (6). Since the measured bin counts can be treated as nearly independent Poisson distribution, the covariances of measured bin counts can be approximately expressed to

$$\mathrm{Cov}[E_i, E_j] = \delta_{ij} E_i. \tag{13}$$

The total uncertainties including unfolding errors are from 2.6% to 15%, as shown by the red curve in Fig. 17 and displayed as the violet error band in Figs. 15 and 16. The unfolding uncertainties are also taken into account in the fission cross section ratios, as shown in Fig. 14.

VI. CONCLUSION

A new measurement of the ^{239}Pu fission cross section relative to ^{235}U was carried out at CSNS Back-n. The measured results generally agree with the evaluations and other experimental data within the margin of the uncertainty from 4 keV to 1 MeV, especially from 150 keV to 1 MeV. However, the measured results exhibit discrepancies with the evaluations from 30 MeV to 80 MeV. Our data slightly are higher than the evaluations and other experimental data in the multichance fission plateaus. The influence of the different active area between the ^{239}Pu and ^{235}U samples is non-negligible, as well as the influence of the nonstandard ^{235}U(n, f) cross section from 4 keV to 150 keV. The ^{239}Pu(n, f) cross sections from 4 keV to 100 MeV relative to ^{235}U(n, f) are obtained with uncertainties from 1.7% to 5.8%. To reflect the effect of the double-bunch running mode in the results, the uncertainties including the unfolding errors are also provided as references. They are 2.6–15% from 10 keV to 100 MeV. Additionally, the ^{239}Pu(n, f) cross section is analyzed by using the nuclear reaction theoretical model and calculation program TALYS 1.95.

The result confirms current evaluations in most energy points and provides discrepant experiment data in the second chance and third chance fission energy regions.

In addition, we plan to carry out another experiment next time under a better experimental condition and in the single-bunch mode when it is possible.

ACKNOWLEDGMENTS

This work was supported by the Key Laboratory of Nuclear Data foundation (Grant No. 6142A08180403) and National Natural Science Foundation of China (Grant Nos. 11790321 and 11905031) and Youth Innovation Promotion Association CAS. We wish to acknowledge Jianqi Chen from Great Bay University for the helpful review and editing for the manuscript.

[1] G. Aliberti, G. Palmiotti, M. Salvatores, T. K. Kim, T. A. Taiwo, M. Anitescu, I. Kodeli, E. Sartori, J. C. Bosq, and J. Tommasi, Ann. Nucl. Energy **33**, 700 (2006).
[2] G. W. Carlson and J. W. Behrens, Nucl. Sci. Eng. **66**, 205 (1978).
[3] P. Staples and K. Morley, Nucl. Sci. Eng. **129**, 149 (1998).
[4] O. Shcherbakov, A. Donets, A. Evdokimov, A. Fomichev, T. Fukahori, A. Hasegawa, A. Laptev, V. Maslov, G. Petrov, S. Soloviev *et al.*, J. Nucl. Sci. Technol. **39**, 230 (2002).
[5] F. Tovesson and T. S. Hill, Nucl. Sci. Eng. **165**, 224 (2010).
[6] Q. An, H. Y. Bai, J. Bao, P. Cao, Y. Chen, Y. L. Chen, P. J. Cheng, R. R. Fan, C. Q. Feng, J. Gu *et al.*, J. Instrumentation **12**, P07022 (2017).
[7] T. Jing-Yu, F. Shi-Nian, J. Han-Tao, T. Hong-Qing, W. Jie, and X. Hai-Hong, Chin. Phys. C **34**, 121 (2010).
[8] H. T. Jing, J. Y. Tang, H. Q. Tang, H. H. Xia, T. J. Liang, Z. Y. Zhou, Q. P. Zhong, and X. C. Ruan, Nucl. Instrum. Methods Phys. Res. A **621**, 91 (2010).
[9] Y. Chen, G. Luan, J. Bao, H. Jing, L. Zhang, Q. An, H. Bai, P. Cao, Q. Chen, P. Cheng *et al.*, Eur. Phys. J. A **55**, 115 (2019).
[10] Y. Yang, Z. Wen, Z. Han, M. Wang, R. Liu, J. Wen, X. Liu, and Y. Chen, Nucl. Instrum. Methods Phys. Res. A **940**, 486 (2019).
[11] Q. Wang, P. Cao, X. Qi, T. Yu, X. Ji, L. Xie, and Q. An, Rev. Sci. Instrum. **89**, 013511 (2018).
[12] I. Antcheva, M. Ballintijn, B. Bellenot, M. Biskup, R. Brun, N. Buncic, P. Canal, D. Casadei, O. Couet, V. Fine *et al.*, Comput. Phys. Commun. **180**, 2499 (2009).
[13] H. Yi, T. F. Wang, Y. Li, X. C. Ruan, J. Ren, Y. H. Chen, Q. Li, J. Wen, J. Y. Tang, Q. An *et al.*, J. Instrum. **15**, P03026 (2020).
[14] S. Agostinelli, J. Allison, K. Amako, J. Apostolakis, H. Araujo, P. Arce, M. Asai, D. Axen, S. Banerjee, G. Barrand *et al.*, Nucl. Instrum. Methods Phys. Res. A **506**, 250 (2003).
[15] D. A. Brown, M. B. Chadwick, R. Capote, A. C. Kahler, A. Trkov, M. W. Herman, A. A. Sonzogni, Y. Danon, A. D. Carlson, M. Dunn *et al.*, Nucl. Data Sheets **148**, 1 (2018).
[16] M. B. Chadwick, M. Herman, P. Oblozinsky, M. E. Dunn, Y. Danon, A. C. Kahler, D. L. Smith, B. Pritychenko, G. Arbanas, R. Arcilla *et al.*, Nucl. Data Sheets **112**, 2887 (2011).
[17] Y. Watanabe, K. Kosako, S. Kunieda, S. Chiba, R. Fujimoto, H. Harada, M. Kawai, F. Maekawa, T. Murata, H. Nakashima *et al.*, J. Korean Phys. Soc. **59**, 1040 (2011).
[18] A. J. Koning, D. Rochman, J. C. Sublet, N. Dzysiuk, M. Fleming, and S. van der Marck, Nucl. Data Sheets **155**, 1 (2019).
[19] Z. Ge, R. Xu, H. Wu, Y. Zhang, G. Chen, Y. Jin, N. Shu, Y. Chen, X. Tao, Y. Tian *et al.*, EPJ Web Conf. **239**, 09001 (2020).
[20] O. Cabellos, F. Alvarez-Velarde, M. Angelone, C. J. Diez, J. Dyrda, L. Fiorito, U. Fischer, M. Fleming, W. Haeck, I. Hill *et al.*, EPJ Web Conf. **146**, 06004 (2017).
[21] A. V. Ignatyuk and B. I. Fursov, in *International Conference on Nuclear Data for Science and Technology* (EDP Sciences, France, 2007), pp. 759–763, https://10.1051/ndata:07641.
[22] A. J. Koning, S. Hilaire, and M. C. Duijvestijn, AIP Conf. Proc. **769**, 1154 (2005).
[23] L. Zhang, Ph.D. thesis, University of Science and Technology of China (2018), https://kns.cnki.net/kcms/detail/detail.aspx?dbcode=CDFD&dbname=CDFDLAST2018&filename=1018123562.nh&uniplatform=NZKPT&v=uu6f-MzDPP6lW5FSBpj2LGMJDtzi2siH7TbOp98u6e92QOo8c LECfUsutVa0zusB.
[24] T. Adye, in *Proceedings of the PHYSTAT 2011 Workshop, CERN, Geneva* (2011), pp. 313–318, http://cds.cern.ch/record/1349242.
[25] H. Yi, The CSNS Back-n double-b unfolding program packages and demo code, https://code.ihep.ac.cn/yih/csns-back-n-doublebunchunfolder.